Florida International University

FIU Digital Commons

5-21-2019

Iron oxides as efficient sorbents for CO2 capture

Eduin Yesid Mora Mendoza

Armando Sarmiento Santos

Enrique Vera Lopez

Vadym Drozd

Andriy Durygin

See next page for additional authors

Authors

Eduin Yesid Mora Mendoza, Armando Sarmiento Santos, Enrique Vera Lopez, Vadym Drozd, Andriy Durygin, Jiuhua Chen, and Surendra Saxena

Original Article

Iron oxides as efficient sorbents for CO₂ capture

Eduin Yesid Mora Mendoza [a,b,*], _Armando Sarmiento Santos_ [a], _Enrique Vera López_ [a],
Vadym Drozd [b], _Andriy Durygin_ [b], _Jiuhua Chen_ [b], _Surendra K Saxena_ [b]

[a] _Universidad Pedagógica y Tecnológica de Colombia UPTC, Tunja 150008, Colombia_
[b] _Center for the Study of Matter at Extreme Conditions, College of Engineering and Computing, Florida International University, Miami, FL 33199, USA_

A B S T R A C T

Carbon dioxide capture/release reactions using magnetite, Fe_3O_4, and hematite, Fe_2O_3, as sorbents were studied. Kinetics of mechanically activated chemical reactions between iron oxides and CO_2 was investigated as a function of CO_2 pressure and planetary ball mill process parameters. It was found that complete carbonation of iron oxides can be accomplished at room temperature and elevated CO_2 pressure (10–30 bar). Siderite calcination was studied in vacuum and argon atmospheres. $FeCO_3$ can be decomposed at 367 °C yielding magnetite, carbon and/or iron. This mixture can reversibly re-absorb carbon dioxide in multiple carbonation–calcination cycles. These results suggest that siderite or iron oxides are prospective and efficient reversible sorbents for CO_2 capture.

1. Introduction

The emission of carbon dioxide has been rising for the last several decades as a result of increasing use of fossil fuel by different sectors of industry. According to some recent studies, if the use of fossil fuels continues at this or increasing rate over next 50 years, the CO_2 concentration in the atmosphere could reach 580 ppm [1] causing significant global effects on living organisms and ecosystems. The Kyoto protocol, adopted in 1997, promotes the reduction of emissions of greenhouse gases notably CO_2, which is the main cause of global warming [2]. This treaty has triggered off the development of new and improved technologies of carbon dioxide capture and sequestration.

Current technologies of carbon dioxide capture and sequestration are based on either physical or chemical methods. In physical methods, carbon dioxide is absorbed under different conditions of pressure and temperature by a solid or liquid and is released by the absorbents on decompression and/or heating. The chemical absorption methods are based on chemical reactions between absorbent and carbon dioxide [3–7]. Amine solutions are the most common absorbents. Several studies have shown that amine absorption is costly and energy intensive. Amine systems to capture 90% of the CO_2 from a flue gas of fossil-fuel power plant, could cost up to 30% of the electricity generated by the plant [8,9].

The adsorption and membranes are two other technologies developed, but like absorption due to the huge amount of

---

flue gas, they are not considered as suitable solutions [1,10,11] so far. Researchers have largely focused on improving membrane CO_2/N_2 selectivity, often by using facilitated transport mechanism membranes [12].

Another approach to CO_2 capture that is gaining relevance in the recent years focuses on metal oxides such as CaO, MgO and FeO, which can react with CO_2 yielding metal carbonates. Once the metal carbonates are formed they can be heated to release pure CO_2 gas and regenerate the oxides. Normally carbonation reactions are exothermic and carbonate decomposition reactions are endothermic which allow designing a cyclic process [13–15].

Iron oxides are attractive sorbents for iron mills because they can be carbonated and regenerated several times, and after that, be processed for steel production at the same iron making facility. The steel industry consumes large amount of fossil fuels which makes it one of the most energy-intensive industrial sub-sectors accounting for about 7% of total CO_2 emission [16]. The blast furnace gasses (BFG) are CO, N_2, H_2 and CO_2. The main source of carbon is a coke which generates CO_2 emissions between 17% and 25% of total flow of the gases. Nowadays, CO_2 is captured mainly from the BFG by chemical absorption methods using primary amines [17,18] or physical absorption methods like pressure swing absorption, and vacuum pressure swing absorption [14].

This work presents a study on the capture of CO_2 using iron oxides, synthesizing siderite. Normally, synthetic siderite can be produced either at high pressure and high temperature conditions from iron oxides and ferrous oxalate, or by means of chemical methods [19–23].

It was shown that iron oxides have active sites exposed at the surface which can react with the gaseous molecules of CO_2 [24]. Materials treated in grinding processes decrease in the particle size, forming a new fresh surfaces and creating more active sites which translates to increase of the surface area [25,26]. Iron can be a good reducing agent not only due to its thermodynamic properties but also because it is produced on a site where carbon dioxide capture takes place, steel mill [27]. Therefore, we propose the following initial carbonation reactions:

$$Fe_3O_4(s) + Fe(s) + 4CO_2(g) \rightarrow 4FeCO_3(s) \qquad (1)$$

$$Fe_2O_3(s) + Fe(s) + 3CO_2(g) \rightarrow 3FeCO_3(s) \qquad (2)$$
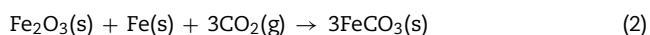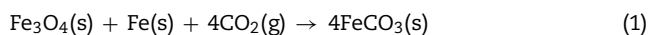
Reactions (1) and (2) allow producing iron(II) carbonate; reaction (1) was previously studied using a thermo-pressure system with additions of water to improve the reaction kinetics [14]. In nature, carbonate minerals are part of different rocks mainly represented by the quaternary system $FeCO_3–MgCO_3–CaCO_3–MnCO_3$. Natural samples of iron carbonate show different amounts of substitutions of Mg, Ca, Mn for Fe in the lattice, which suggests that pure siderite seldom occurs [28]. Natural siderite forms complete series of solid solutions with magnesium and manganese carbonates, while a wide miscibility gap reported between iron and calcium carbonates. Solubility of Ca^{2+} in siderite does not exceed 10 mol.% at 550 °C, while calcite ($CaCO_3$) can contain up to 20 mol.% of Fe^{2+} at the same temperature. Siderite is a commercial

mineral and has many applications such as source of iron in steel industry, raw material in cement industry, hydrogen production, refining of ferrosilicon, shale oil production, etc. [29,30].

The thermal decomposition of siderite is very important issue mainly in processing of oil shales or in the combustion of coals [31,32]. Mechanism of the thermal decomposition of siderite is complicated and depends both on its composition and experimental conditions. Formation of solid solutions between $FeCO_3$ and other metal carbonates increases decomposition temperature of natural siderite samples compared to synthetic one. Temperature, atmosphere, microstructure and heating rate are those experimental parameters which determine phase composition of siderite decarbonation products. In oxygen-rich atmosphere the only end product is hematite, while magnetite, wustite and pure iron could form in vacuum or in an inert atmosphere [28].

There is a remarkable difference in the thermal decomposition behavior of natural and synthetic siderite. For example, Gotor et al., [28] reports that the decomposition temperature of synthetic siderite is approximately 200 K below of the decomposition temperature of the natural sample.

The thermodynamic stability fields of siderite, wustite and magnetite have been studied as a function of P_{CO} and P_{CO_2} at different temperatures [19,33]. It was found that the pressure range of siderite stability is smaller at higher temperatures, on the other hand, the stability pressure of magnetite and wustite is extended at higher temperatures. Existence of siderite at high temperatures is possible only at high P_{CO} and P_{CO_2}; at those conditions the molar ratio of FeO/Fe_3O_4 increases with temperature [33].

FeO formed by mechanic chemical reaction between Fe_2O_3 and Fe can be decomposed into Fe_3O_4 and Fe by an endothermic reaction at 250 °C according to DSC study [34]. Results reported in Ref. [29] confirm that siderite decomposition proceeds through formation of FeO and CO_2 and after that FeO undergoes transformation to Fe and Fe_3O_4. Moreover, several studies have reported carbon (C), oxygen (O), carbon monoxide (CO) [19,30,35–37] as by-products of siderite decomposition at different experimental conditions.

In order to obtain a reducing agent after calcination, siderite decomposition was studied in inert atmosphere, hence, the magnetite regeneration reactions are shown below:

$$6FeCO_3(s) \rightarrow 2Fe_3O_4(s) + C(s) + 5CO_2(g) \qquad (3)$$

$$4FeCO_3(s) \rightarrow Fe_3O_4(s) + Fe(s) + 4CO_2(g) \qquad (4)$$
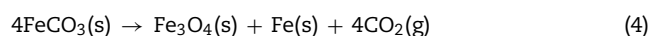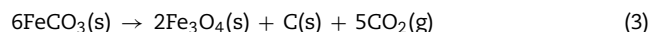
Products of siderite decomposition, Fe_3O_4, Fe and/or C are decarbonated sorbent which can re-absorb carbon dioxide, e.g.:

$$2Fe_3O_4(s) + C(s) + 5CO_2(g) \rightarrow 6FeCO_3(s) \qquad (5)$$
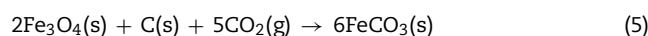
Hence, initial material (Fe_3O_4/Fe_2O_3 + Fe) can be used for multiple cycles according to the combination of (1)–(5) reactions, as can be seen in Fig. 1. Carbon has the advantage that it is cheaper than iron.
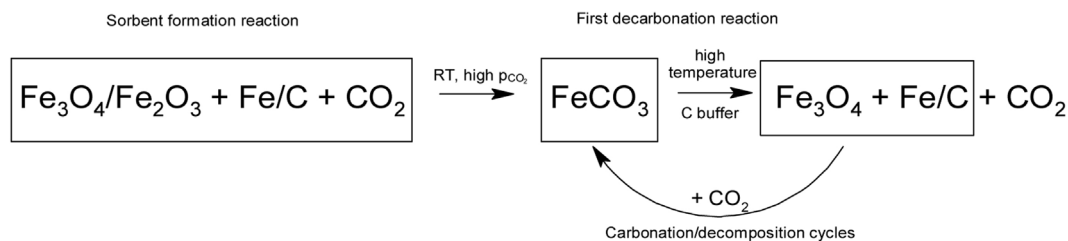
Sorbent formation reaction

First decarbonation reaction

$$Fe_3O_4/Fe_2O_3 + Fe/C + CO_2 \xrightarrow{RT,\, high\, p_{CO_2}} FeCO_3 \xrightarrow[C\, buffer]{high\, temperature} Fe_3O_4 + Fe/C + CO_2$$

+ CO₂

Carbonation/decomposition cycles

Fig. 1 – Suggested scheme of carbon dioxide capture via siderite.

2. Experimental

Mechanochemical reactions between magnetite or hematite and carbon dioxide were performed at room temperature and elevated CO_2 pressure (10–30 bar). Planetary ball mill Retsch PM100 was operated at 200–400 rpm. Vessel for the ball milling was a stainless-steel jar of 50 mL volume capable for holding up to 100 bar gas pressure. High purity CO_2 gas (Airgas, 99.999%) was loaded into the reactor at different pressures together with 3.00 g of magnetite (Alfa Aesar, nanopowder, 97%) or hematite (99.945%) and iron (Good Fellow, 99% purity, <60 µm) mixture in a molar ratio 1:1. The powder to balls (stainless steel) weight ratio was 2:27. Reactor was flushed several times with CO_2 gas to ensure a pure CO_2 atmosphere inside the reactor. Mechanochemical reaction was run for different periods of time from 30 min up to 36 h. Each 1 h milling interval was followed by half an hour cooling interval to avoid overheating of the sample.

Thermogravimetric analysis (TGA) and differential scanning calorimetry (DSC) were conducted in a temperature range of 25–1000 °C using TA Instruments SDT Q600 instrument. The measurements were performed in air and Ar atmospheres with a heating rate of 10 °C/min. Powder X-ray diffraction patterns were collected using Bruker GADDS/D8 diffractometer equipped with Apex Smart CCD Detector and molybdenum rotating anode. Collected 2D diffraction patterns were integrated using Fit2D software [38]. Quantitative phase analysis of the samples was performed using Rietveld method and GSAS package [39,40]. The CO_2 sorption capacity was calculated using the results generated by Rietveld refinement of XRD patterns. Scanning electron microscope (JEOL JSM-6330F) was used to study the morphology of powder particles. Surface area of the powders was measured using Brunauer–Emmett–Teller (BET) method and Micromeritics Tristar II 3020 instrument. Raman spectroscopy characterization was used to identify carbon in siderite decomposition products. A continuous wave (CW) argon ion (Ar^+) laser (model 177G02, Spectra Physics) of 514.4 nm in wavelength was used as a source of monochromatic radiation. Backscattered Raman spectra were collected by a high-throughput holographic imaging spectrograph (model HoloSpec f/1.8i, Kaiser Optical Systems) with volume transmission gratings, a holographic notch filter, and thermoelectrically cooled charge-coupled device (CCD) detector (Andor Technology). The Raman system has spectral resolution of 4 cm^{-1}. The spectra were usually collected with 10 min exposure.

3. Results

3.1. Thermodynamic simulation of Fe_3O_4–Fe–CO_2 and Fe_2O_3–Fe–CO_2 systems

FACTSAGE software and the databases therein, FACT – F*A*C*T 5.0, SGPS – SGTE and SGSL [41] were used to verify the thermodynamic feasibility of carbonation process for the systems Fe_3O_4–Fe–CO_2 and Fe_2O_3–Fe–CO_2. Fig. 2 shows the calculated equilibrium temperature as a function of pressure (phase diagram) in both systems. These results indicate that the siderite formation is favored either by high pressures at a constant temperature or by low temperatures at a constant pressure. Both systems have similar behavior. The Fe_2O_3–Fe–CO_2 system shows slightly lower equilibrium temperatures at the same pressure. This calculation indicates that carbonation is thermodynamically favorable during ball milling process at room temperature and decarbonation is possible at relatively low temperatures (about 180 °C at 1 atm pressure).

3.2. Siderite formation through ball milling

Fig. 3 illustrates kinetics of iron(II) carbonate formation in mechanochemical reaction between magnetite and iron at 30 bar CO_2 pressure and 400 rpm planetary ball mill revolution speed. Weak diffraction peaks of $FeCO_3$ are detected after 30 min milling interval and their intensities increase with milling time. Diffraction peaks of elemental iron vanish after 2 h of milling while Fe_3O_4 phase persists for 15 h of the reaction. Disappearance of Fe diffraction peaks but not those of magnetite in XRD patterns could be an indication of elemental iron amorphization on early stage of ball milling. The 36 h sample reveals the presence of siderite as a major phase and small amount of magnetite. Theoretical CO_2 absorption capacity of Fe_3O_4–Fe mixture in 1:1 molar ration is 0.6126 g CO_2/g sorbent. Rietveld refinement of XRD pattern of 36 h sample yields siderite content 99.76% which is equivalent to 0.6101 g CO_2/g sorbent capacity. CO_2 absorption capacity which was calculated from TG experiment (see Section 3.3) is 0.5213 g CO_2/g sorbent. The difference is associated with small oxidation that occurs in TG when the regenerated oxides come into contact with CO_2 when it is released.

According to Ref. [28] synthetic siderite crystallizes in hexagonal space group R-$3c$ with lattice parameters $a = b = 4.6919(8)$ Å and $c = 15.407(2)$ Å. Calculated lattice
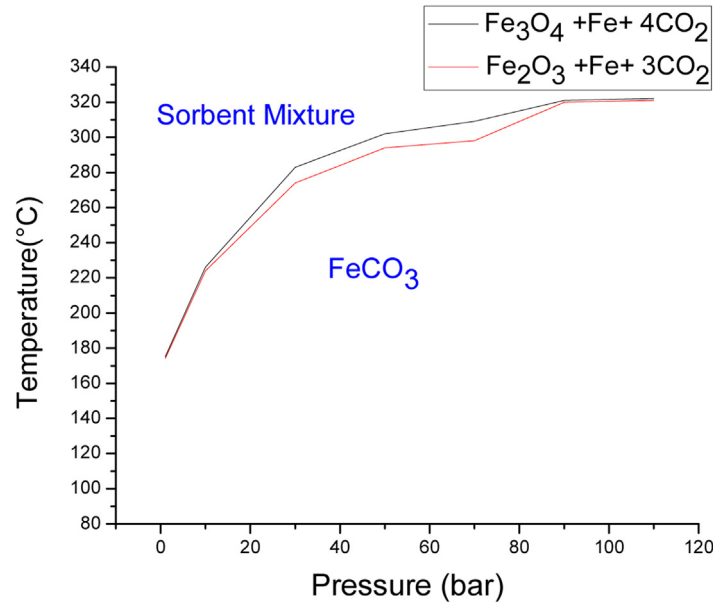
Fig. 2 – Equilibrium temperature of siderate decomposition as a function of pressure for the systems $Fe_3O_4 + Fe + 4CO_2 \rightarrow 4FeCO_3$ and $Fe_2O_3 + Fe + 3CO_2 \rightarrow 3FeCO_3$.
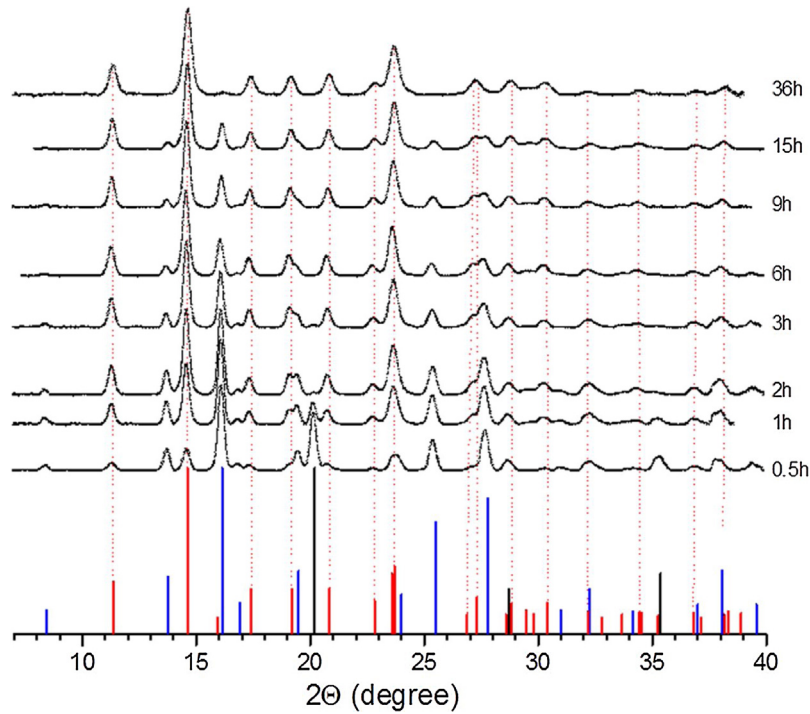

Fig. 3 – Evolution of X-ray diffraction patterns ($\lambda = 0.71073$ Å) of $Fe_3O_4 + Fe$ mixture at 30 bar CO_2 pressure with a time of ball milling (400 rpm). Plot at the bottom shows XRD patterns of Fe (JCPDS #006-0696; black), Fe_3O_4 (JCPDS #001-1111; blue) and $FeCO_3$ (JCPDS #029-0696; red). Red dotted lines show positions of the diffraction peaks of siderite.

parameters of siderite in this study are $a = b = 4.679(3)$ Å and $c = 15.281(7)$ Å which agree with reported values.

Broadening of diffraction peaks of siderite during milling indicates about crystallite size reduction. Average crystallite size of $FeCO_3$ in 36 h sample estimated using Scherrer's formula is 82 Å.

The energy spent in ball milling process can be calculated. According to Burgio et al. [42], the transferred energy to a mass,

Et_m, in a planetary ball milling can be obtained as a function of filling factor in the jar, ϕ, ball mass, m_b, ball diameter, d_b, number of balls, N_b, reaction time, t, angular rotation speeds of plate and jar, W_p and W_v, radius of plate and jar, R_p and R_v and sample mass, PW, as follows:

$$Et_m = \phi N_b m_b t (W_p - W_v) \left[\frac{W_v^3 (R_v - (d_b/2))}{W_p + W_p W_v R_p} \right] \left(\frac{(R_v - d_b/2)}{2\pi PW} \right) \quad (6)$$
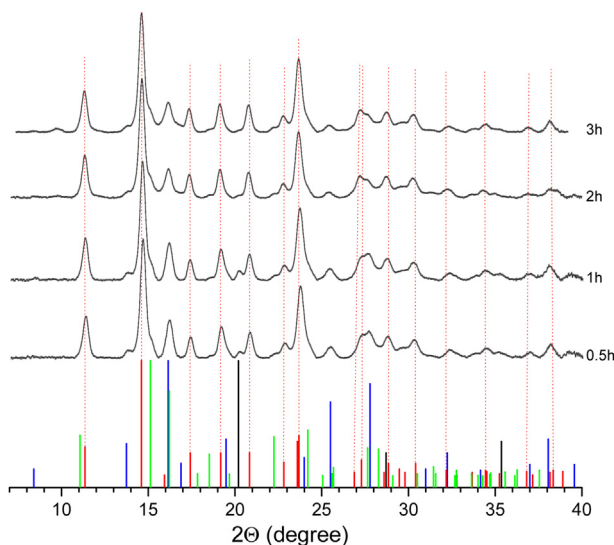
Fig. 4 – Evolution of XRD patterns (λ = 0.71073 Å) of Fe_2O_3 + Fe mixture during ball milling (400 rpm) at 30 bar CO_2 pressure. Plot at the bottom shows XRD patterns of Fe (JCPDS #006-0696; black), Fe_2O_3 (JCPDS #089-2810; green), Fe_3O_4 (JCPDS #001-1111; blue) and $FeCO_3$ (JCPDS #029-0696; red). Red dotted lines show positions of the diffraction peaks of siderite. (For interpretation of the references to color in this figure legend, the reader is referred to the web version of the article.)
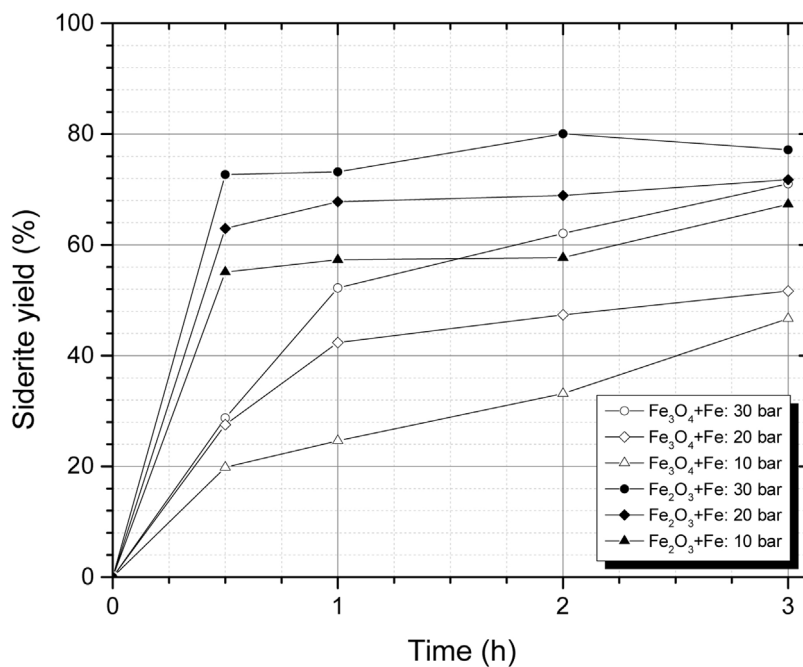

Fig. 5 – Siderite yield as a function of reaction time at 400 rpm for 30, 20 and 10 bars of CO_2 pressure in the Fe_3O_4–Fe–CO_2 and Fe_2O_3–Fe–CO_2 systems.

Here, to obtain siderite, at conditions of 30 bar, 400 rpm and 36 h, the spent of energy is 168.746 W h/g. Taking into account that siderite formation kinetics is faster while metallic iron is present, the material could be initially carbonated for 3 h, spending 14.062 W h/g, thus achieving a CO_2 capture capacity of 8.397 mmol CO_2/g sorbent, which translates to 60.234% of conversion. Sorbent performance in subsequent carbonation cycles improves due to reduction of particle size (see Section 3.4). In industrial processes, the demand for energy can be supplied by renewable energy sources.

Fig. 4 shows evolution of XRD patterns in the Fe_2O_3–Fe–CO_2 system during ball milling at 30 bar CO_2 pressure, 400 rpm and 0.5–3 h of reaction time. Formation of siderite in this system proceeds through Fe_3O_4 as an intermediate phase. It was shown [34] that hematite quickly converts to magnetite in mechanical ball milling process.

Formation of siderite has strong dependence on CO_2 pressure. Fig. 5 depicts siderite yield at different CO_2 pressures as a function of reaction time for two systems. Iron(II) carbonate yield increases with CO_2 pressure and reaction time.
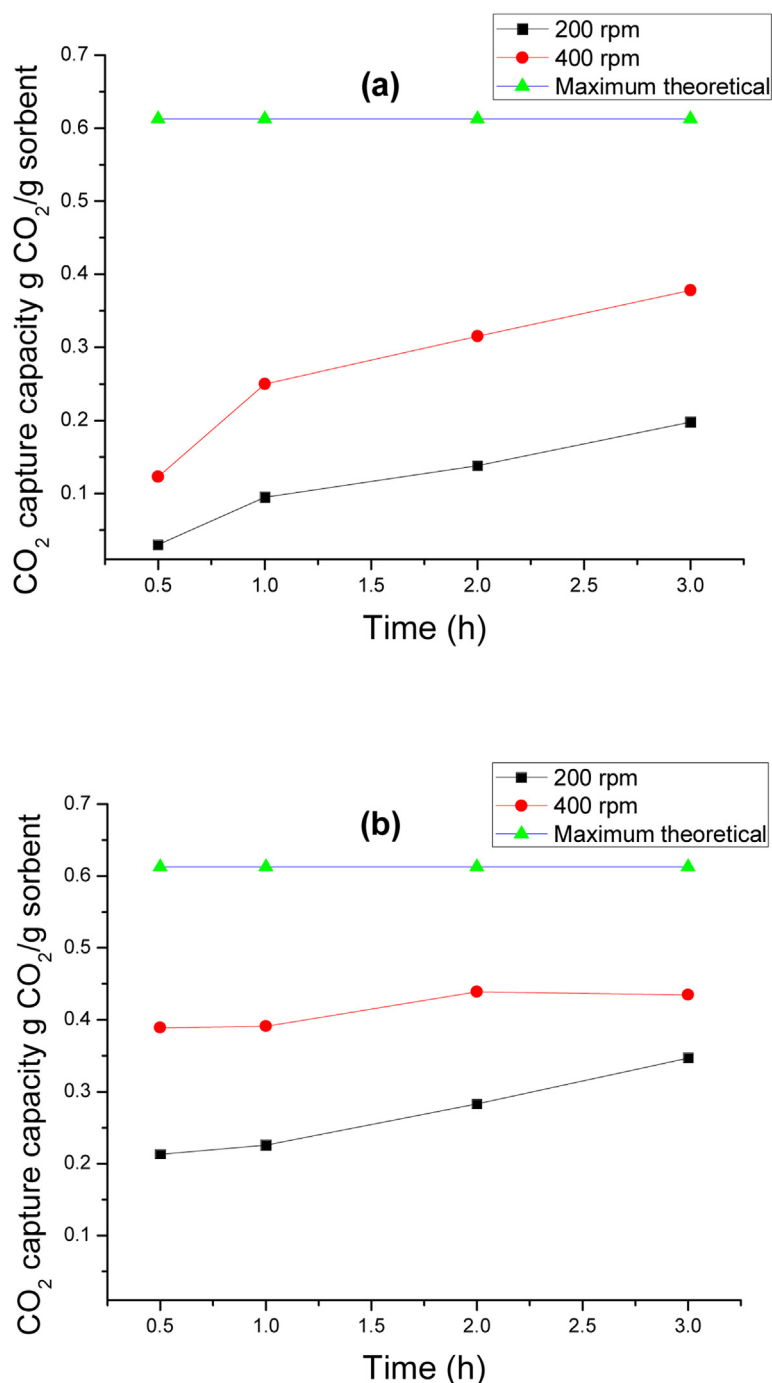
Fig. 6 – CO$_2$ capture capacity as a function of reaction time for 200 and 400 rpm at 30 bar in (a) Fe$_3$O$_4$–Fe–CO$_2$ system and (b) Fe$_2$O$_3$–Fe–CO$_2$ system.

Porous solid materials have interconnected pathways where gas molecules collide between them or with the pore walls. If the CO$_2$ gas pressure is high, the molecules can remain within each available pore of magnetite, hematite or iron forming FeCO$_3$. On the other hand, if the pressure is low, collisions between the CO$_2$ molecule and pore walls are dominant and the free path is restricted with the geometry of void space [43,44]. Initially, the CO$_2$ capture kinetics is faster in hematite system and at longer times, the siderite yield trends to stabilize, because of inverse reaction occurs at those conditions.

In mechanical ball milling, the reaction kinetics is strongly affected by revolution speed. Fig. 6 depicts CO$_2$ capture capacity of material for revolution speeds of 200 and 400 rpm as a function of reaction time for the two studied systems. According to these results, if the number of revolutions is lower, the siderite formation decreases; this behavior is observed in both systems. It suggests that, increase in revolution speed transfer higher kinetic energy to the materials promoting formation of crystal defects such as stacking faults, dislocations, vacancies, and increased number of grain boundaries [45–48].

The presence of these defects generates more active sites in magnetite, hematite and iron which facilitates their reaction with CO_2. In a planetary ball mill, increasing the speed of rotation will increase the speed with which the balls move. Above a critical speed, the balls will be pinned to the inner walls of the jar and do not fall down to exert any impact force. Therefore, the maximum speed should be just below this critical value so that the balls fall down from the maximum height to produce the maximum collision energy [48]. It is clear that for the studied conditions, 200 and 400 rpm are below such a critical speed. Here faster speeds were not used because of industrial processes limitations.

3.3. TG/DSC study of siderite decomposition

Siderite decomposition reactions were studied on a sample of pure siderite obtained at 30 bar CO_2 pressure, 400 rpm and 36 h in the system Fe_3O_4–Fe–CO_2. The calcination temperature (absorbent regeneration) of siderite was experimentally identified using thermogravimetrical analysis.
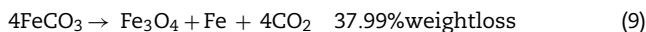
According to the literature a two-step mechanism of decomposition of $FeCO_3$ is established. Formation of non-stoichiometric wüstite, FeO, in the first step of decomposition is followed by its transformation to other products depending on the experimental conditions, oxygen partial pressure, in particular.

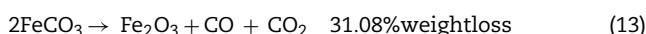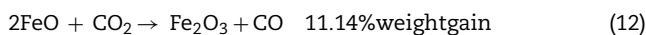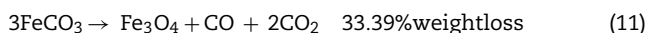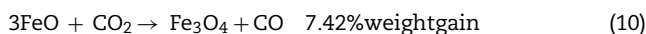$$FeCO_3 \rightarrow FeO + CO_2 \quad 37.99\%\text{weightloss} \quad (7)$$
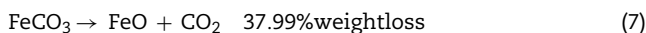
Second-step reactions are listed below in order of increasing oxygen partial pressure. Wüstite is not thermodynamically stable below 563 °C and undergoes in a vacuum or inert atmosphere a disproportionation reaction, e.g. [34]:
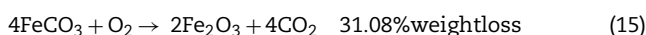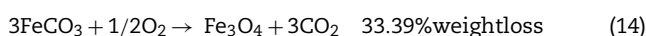
$$4FeO \rightarrow Fe_3O_4 + Fe \quad \text{noweightchange} \quad (8)$$
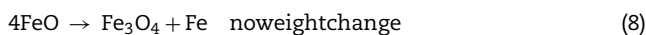
Overall reaction of reactions (6) and (7):

$$4FeCO_3 \rightarrow Fe_3O_4 + Fe + 4CO_2 \quad 37.99\%\text{weightloss} \quad (9)$$

Wüstite also can be oxidized by carbon dioxide produced in the reaction (7) according reactions (10) and (12). Decomposition reactions of siderite (11) and (13) can also generate carbon dioxide:

$$3FeO + CO_2 \rightarrow Fe_3O_4 + CO \quad 7.42\%\text{weightgain} \quad (10)$$

$$3FeCO_3 \rightarrow Fe_3O_4 + CO + 2CO_2 \quad 33.39\%\text{weightloss} \quad (11)$$

$$2FeO + CO_2 \rightarrow Fe_2O_3 + CO \quad 11.14\%\text{weightgain} \quad (12)$$

$$2FeCO_3 \rightarrow Fe_2O_3 + CO + CO_2 \quad 31.08\%\text{weightloss} \quad (13)$$

In the presence of oxygen, oxidation of $FeCO_3$ takes place very rapidly, yielding hematite or magnetite (in moderately oxidative atmosphere):

$$3FeCO_3 + 1/2O_2 \rightarrow Fe_3O_4 + 3CO_2 \quad 33.39\%\text{weightloss} \quad (14)$$

$$4FeCO_3 + O_2 \rightarrow 2Fe_2O_3 + 4CO_2 \quad 31.08\%\text{weightloss} \quad (15)$$

Moreover, it is worth to mention one more $FeCO_3$ decomposition pathway which was experimentally observed at low oxygen partial pressure in the presence of the graphite buffer [19]:

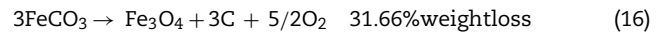$$3FeCO_3 \rightarrow Fe_3O_4 + 3C + 5/2O_2 \quad 31.66\%\text{weightloss} \quad (16)$$

Fig. 7(a) shows the TG/DCS plot for the siderite decomposition in argon atmosphere. Endothermic peak at 367 °C can be assigned to the first step of siderite decomposition. According to TG plot the weight loss in the first step of siderite decomposition is 34.27% which is lower than predicted by reaction (7) 37.99%. The difference is due to the presence of small amount of unreacted Fe and Fe_3O_4. This amount can be calculated from TG curve of siderite decomposition in air atmosphere (Fig. 7(b)). Decomposition of $FeCO_3$ in air atmosphere is accompanied by iron oxidation to Fe_2O_3 according to reaction (15). Theoretical weight loss in this reaction is 31.08%. Fig. 7(b) shows TG curve of $FeCO_3$ decomposition in air atmosphere. Experimental weight loss is 30.68% and it is less than theoretical one. Siderite which was used in this TG experiment was produced by ball milling of equimolar mixture of Fe_3O_4 and Fe at 30 bar CO_2 pressure for 36 h. Difference between theoretical and measured weight loss in reaction (15) must be related to the presence in the siderite sample of unreacted equimolar mixture of Fe_3O_4 and Fe. Oxidation of both Fe and Fe_3O_4 are accompanied by the weight gain and the difference between theoretical and measured weight change in reaction (15) can be used to calculate amount of unreacted iron and magnetite. Calculations show that siderite contains 0.95 wt.% of equimolar mixture of Fe and Fe_3O_4.

If we take into account 0.95 wt.% of Fe + Fe_3O_4 as impurity in the siderite, the first decomposition step in argon atmosphere should be accompanied by 37.63% weight loss which is still larger than observed experimentally for siderite decomposition in Ar atmosphere loss of 34.27%. This evidences that simultaneously to the reaction of FeO formation from siderite and its disproportionation to Fe and Fe_3O_4, oxidation of FeO by CO_2 must occur according either to reaction (10) or (12). Reaction (16) also should be considered as a possible pathway of $FeCO_3$ decomposition. Fe and Fe_3O_4 are stable below 550 °C and react with each other above 550 °C yielding FeO. Thus, endothermic peak observed on DSC curve in Ar atmosphere at 566 °C can be assigned to FeO re-formation from Fe_3O_4 and Fe [33,34,49]. Small weight loss of 1.95% which is accompanied by observed endothermic peak at 668 °C could be related to Fe_2O_3 reduction by carbon [50]. Most of the reports on thermal decomposition of siderite refer to the natural mineral samples which are essentially solid solutions with Ca, Mg, and Mn carbonates. As it was mentioned earlier these impurities affect siderite decomposition temperature and kinetics. One of the rare reports on decomposition of synthetic $FeCO_3$ is by Gotor et al. [28]. They found that natural siderite with $(Fe_{0.7}Mg_{0.3})CO_3$ composition decomposition obeys n-order kinetic model and the synthetic one could be described by an Avrami–Erofeev law. Also, difference in the final decomposition products was observed. Natural siderite sample yields wustite phase of the composition $Fe_{0.7}Mg_{0.3}O$ and small amount of magnetite while products of synthetic siderite sample decomposition are magnetite and iron. Thermal decomposition of natural
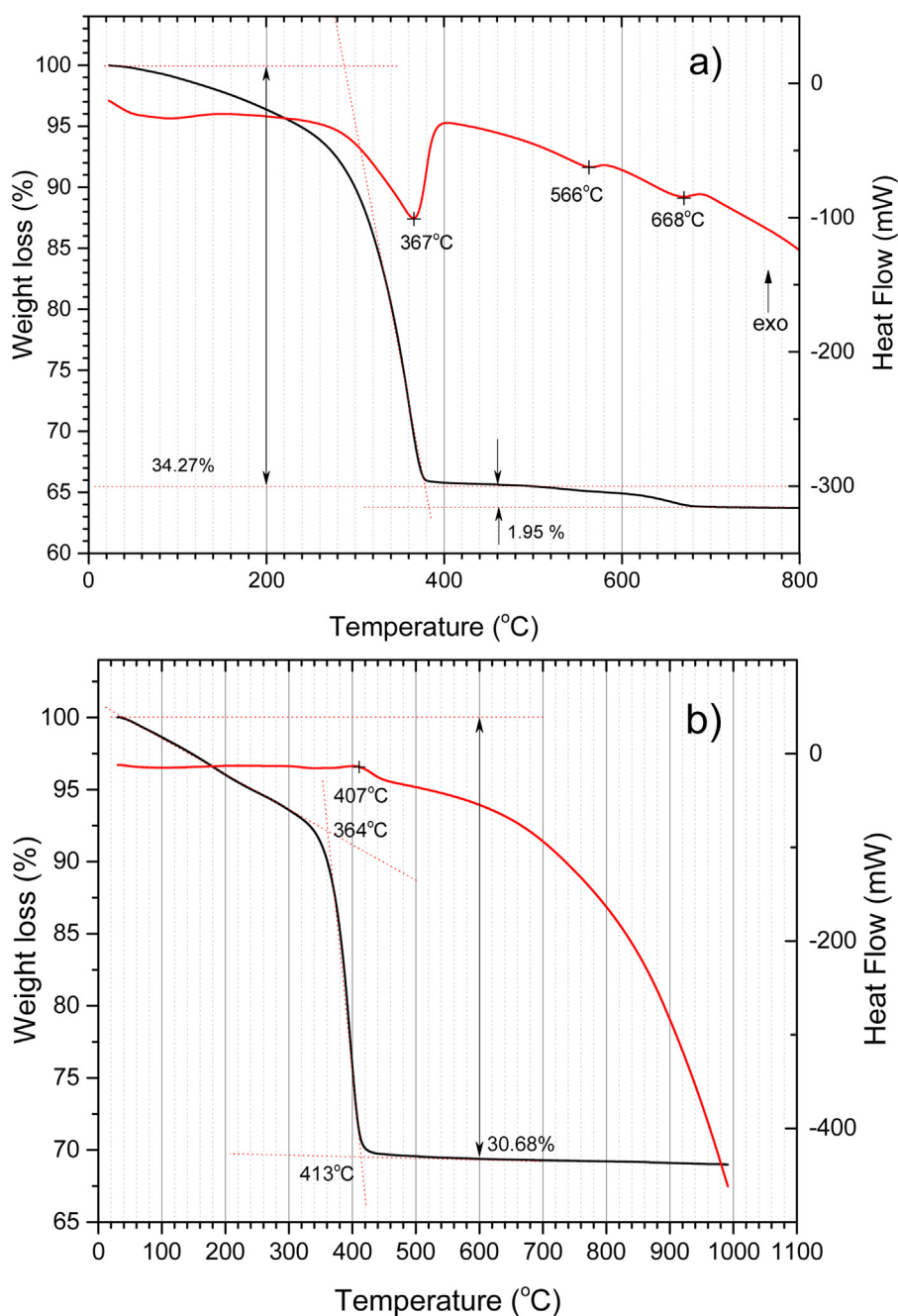
Fig. 7 – TG (black line)–DSC (red line) curves of siderite (formed in Fe$_3$O$_4$ + Fe reaction at 30 bar CO$_2$ pressure, 400 rpm, 36 h) in Ar (a) and air (b) atmospheres at 10 °C/min heating rate. (For interpretation of the references to color in this figure legend, the reader is referred to the web version of the article.)

siderite in air atmosphere is reported in the temperature range 465–550 °C (exothermic peak at 525 °C) [51], 478–580 °C (exothermic peak at 539 °C) [33]. In the inert atmosphere decomposition temperature shifts to slightly higher temperature 438–540 °C (endothermic peak at 500 °C) [33]. Kinetics of thermal decomposition of siderite in air atmosphere obeys three-dimensional diffusion model [33].

According to the thermogravimetric analysis, the siderite decomposition and therefore the release of carbon dioxide occurs in the temperature range 300–400 °C. Total weight loss

in this range of temperature is 34.27%, translating the CO$_2$ capture capacity of sorbent at that conditions to 0.5213 g CO$_2$/g sorbent or 11.84 mmol CO$_2$/g sorbent; this value is relatively close to the theoretical maximum which is 13.91 mmol CO$_2$/g sorbent, demonstrating the high feasibility to capture CO$_2$ by mechanical ball milling method. In Fig. 8 the X-ray diffraction patterns of the products of siderite decomposition in Ar atmosphere and vacuum are shown. It was found that siderite starts decomposing above 300 °C in Ar atmosphere and above 200 °C in vacuum. Magnetite is detected as decomposition product
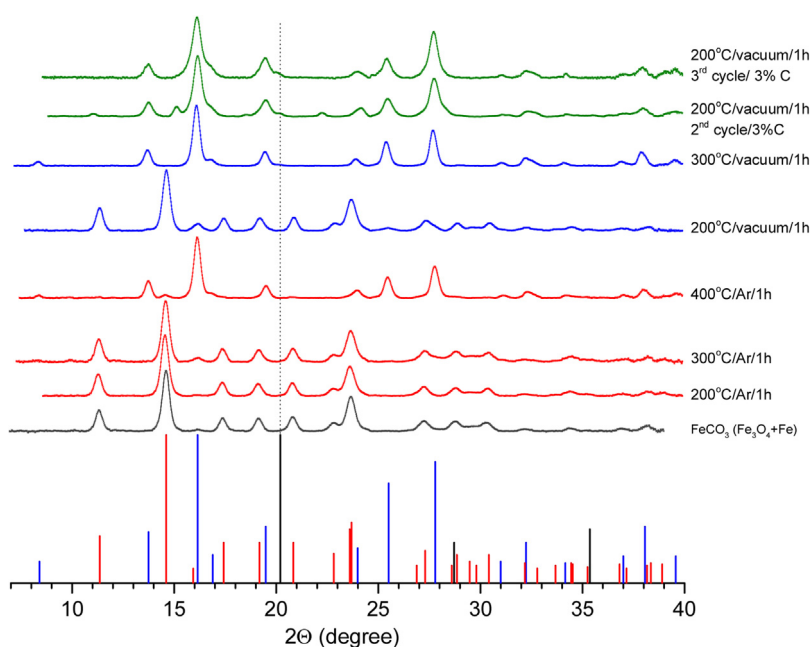
Fig. 8 – X-ray diffraction patterns (λ = 0.71073 Å) of the products of siderite decomposition in Ar atmosphere and vacuum. Plot at the bottom shows XRD patterns of Fe (JCPDS #006-0696; black), Fe_3O_4 (JCPDS #001-1111; blue) and $FeCO_3$ (JCPDS #029-0696; red). Red dotted lines show positions of the strongest diffraction peaks of siderite. (For interpretation of the references to color in this figure legend, the reader is referred to the web version of the article.)

of siderite in both conditions, and metallic iron is identified at vacuum. In addition to XRD decomposition product were also characterized by Raman spectroscopy to test the presence of elemental carbon which could form in $FeCO_3$ thermolysis reaction (16).

Raman spectroscopy is a very used technique to molecular morphology characterization of carbon materials. It is because of its high sensitivity to highly symmetric covalent bonds with little or no natural dipole moment. The carbon–carbon bonds that make up these materials fit this criterion perfectly and as a result Raman spectroscopy is highly sensitive to these materials and able to provide a wealth of information about their structure. Every band in the Raman spectrum corresponds directly to a specific vibrational frequency of a bond within the molecule [52,53]. The 1582 cm^{-1} band of graphite is known as the G band [52,53]. Raman vibration at 1370 cm^{-1} is disorder-induced mode of graphite (D mode) [53]. Fig. 9 shows Raman spectra of the products of siderite decomposition at 200 °C and 300 °C in vacuum. Characteristic peaks of graphite at 1582 cm^{-1} and 1370 cm^{-1} observed in this spectra confirm presence of graphite in decomposition product.

Metallic iron is one of the products of siderite decomposition in vacuum. This fact agrees with the earlier discussed mechanism and with Refs. [28–30] which report FeO as intermedium product of siderite thermolysis.

3.4. Carbonation–calcination cycles

Products of siderite decomposition were subsequently cycled in CO_2 absorption/release reactions. It was found that the capture capacity of the sorbent in the second carbonation cycle is significantly reduced due to the low content of reducing

agent (Fe and C) in the mixture. Reducing agent deficiency was compensated by adding to the sorbent carbon in the form of graphite. XRD patterns of the products which are formed in the second carbonation cycle with different amounts of graphite are shown in Fig. 10. The carbonation was performed at 400 rpm, 30 bar CO_2 pressure for 20 h in planetary ball mill. Addition 1 mol.% of graphite to the mixture leads to the reduction of Fe_3O_4 to FeO. Very little yield of siderite was detected for 1 mol.% graphite loading. Increase in graphite loading above 3 mol.% facilitates carbonation reaction and as it is evident from Fig. 10. Pure siderite can be obtained in the second carbonation cycle with graphite content 5.00 mol.%. Samples of $FeCO_3$ produced in the second and subsequent carbonation cycles were decomposed at 300 °C in vacuum.

Siderite with a yield close to 95% was formed during third and fourth carbonation–calcination cycles, without addition of any extra reducing agent, which suggests that carbonation at this point is favored by two conditions, first, porosity features of material exposed to grinding treatment and second, the reducing agent yielded in the calcination. Fig. 11(a) shows XRD pattern of the products formed after the fourth cycle of carbonation, and Fig. 11(b) shows the products after calcination at 300 °C in vacuum. The products of fourth CO_2 desorption cycle were identified as Fe_3O_4, Fe, and graphite which suggests that the material can be used in posterior CO_2 absorption/desorption cycles.

Table 1 shows pore volume and surface area of initial mixture of magnetite and iron, after 2 h of milling and after four cycles of carbonation–calcination. The surface area increases as a result of ball milling. Noticeably, the surface area after 4 cycles of carbonation and calcination is more than 15 times
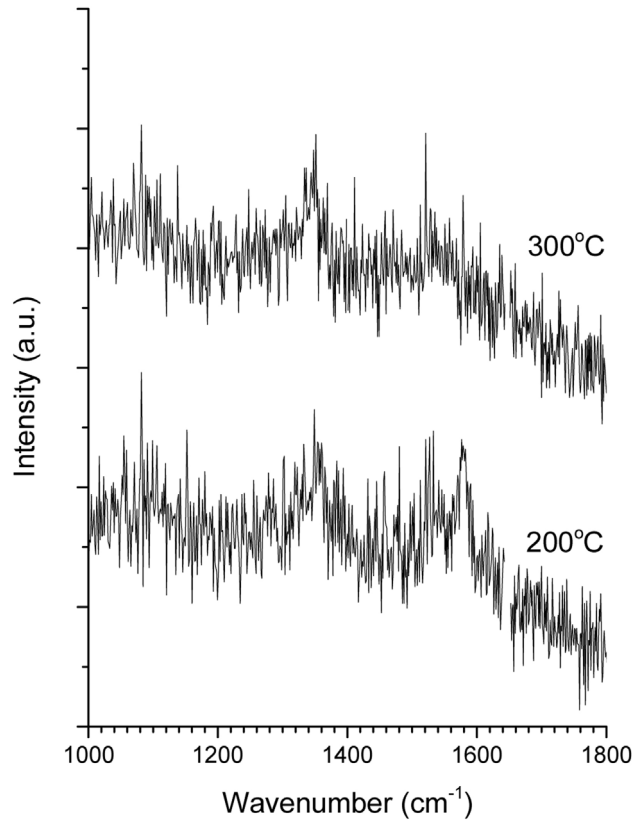
Fig. 9 – Raman patterns of siderite decomposition products at 200 and 300 °C in vacuum.
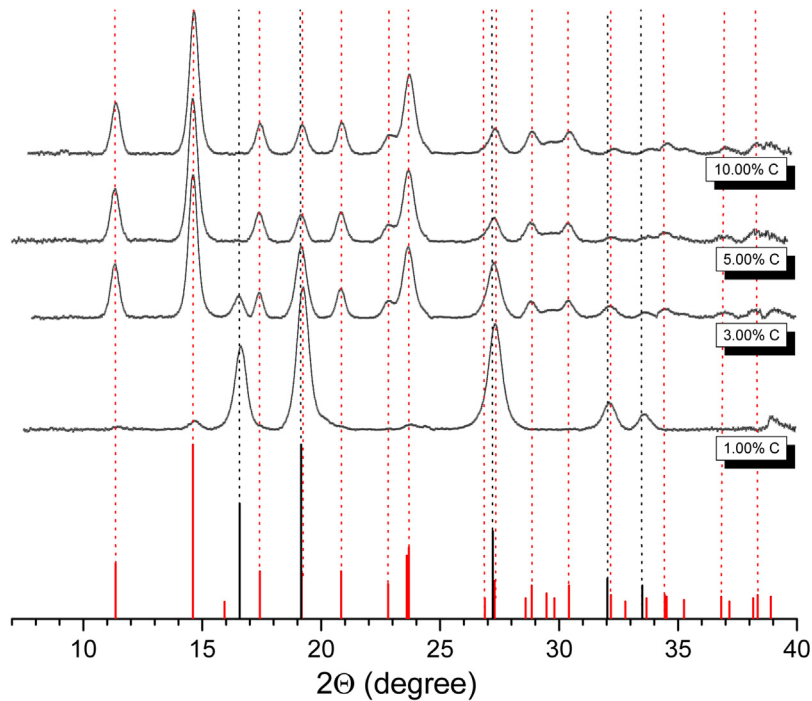

Fig. 10 – XRD patterns ($\lambda = 0.71073$ Å) of the products of the second carbonation cycles with different amounts of extra-graphite. Plot at the bottom shows XRD patterns of FeO (JCPDS #085-0625; black), and FeCO$_3$ (JCPDS #029-0696; red). (For interpretation of the references to color in this figure legend, the reader is referred to the web version of the article.)

Fig. 11 – XRD patterns (λ = 0.71073 Å) of siderite formation products (a) after four cycles of carbonation and (b) products identified after calcination of the fourth cycle. Plot at the bottom shows XRD patterns of Fe$_3$O$_4$ (JCPDS #001-1111; blue), Fe (JCPDS #006-0696; black) and FeCO$_3$ (JCPDS #029-0696; red). (For interpretation of the references to color in this figure legend, the reader is referred to the web version of the article.)
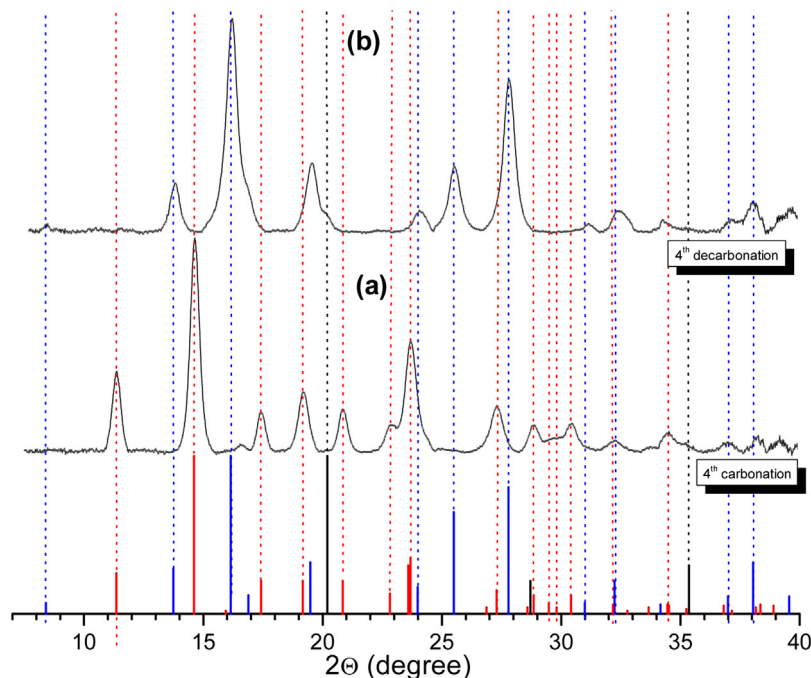
Table 1 – Pore volume and surface area for initial mixture of magnetite and iron, after 2 h of milling and after four carbonation–calcination cycles.

Fe$_3$O$_4$ + Fe	Surface area (m^2/g)	Pore volume (cm^3/g)
Initial mixture	4.66	0.013
2 h milled	16.36	0.045
After four cycles	73.45	0.120

higher than surface area of initial Fe$_3$O$_4$ + Fe mixture. Pore volume also increases with ball milling time.

Additionally, SEM reveals the appearance of material in the three states above mentioned. Fig. 12(a) shows that in the material not treated is possible to identify independently the

particles of iron and magnetite; the iron particles are bigger and have spherical shape. The particle size of Fe$_3$O$_4$ is approximately 300 nm, while for iron the particle size rises 2.5 μm. In the appearance of the milled material for 2 h predominates the agglomeration as is shown in Fig. 12(b); despite of this agglomeration, material is more homogeneous and has larger surface area and pore volume; the particle size of milled material is approximately 380 nm. Bigger particle size and agglomeration in the milled material suggests that the tendency to cold welding predominates over fracture to conditions of 400 rpm revolution speed [45]. The carbonated and calcined material shows high discrepancy in the appearance of the particles, developing a broad range between particles size (0.1–30 μm) as can be seen in Fig. 12(c), indicating that during the process, cold welding predominates over fracture.
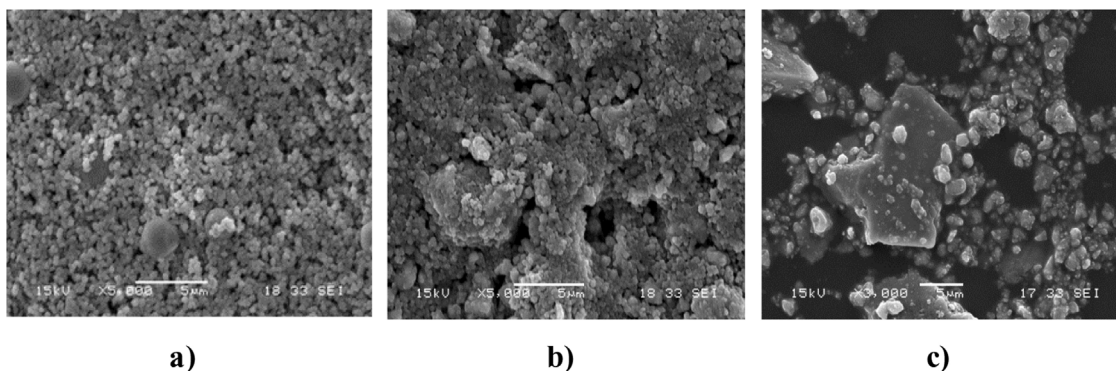

Fig. 12 – SEM images of (a) as received Fe$_3$O$_4$ and Fe (b) 2 h ball milled (c) after four carbonation–calcination cycles at magnification of 5000×, 5000× and 3000×, respectively.

Formation of biggest particles at 400 rpm and long reaction times (more than 20 h per cycle) is due to three factors: (1) the lattice strain falls with the refinement, hence the rate of cold welding is more than the rate of fracturing; (2) strong agglomerating force due to high energy per impact; (3) the ductile nature of iron based components [45].

4. Conclusion

This study presents a novel method to capture CO_2 by mixtures of raw materials used in steel industry (Fe_3O_4 + Fe and Fe_2O_3 + Fe). Increases in siderite formation (CO_2 capture capacity) during planetary ball milling conditions were achieved by increases of pressure, revolution speed of ball milling, and reaction time. Predominantly pure siderite was produced at 30 bar CO_2 pressure, 400 rpm and 36 h of reaction time from Fe_3O_4 and Fe, which yields a CO_2 capture capacity of 0.6101 g CO_2/g sorbent. CO_2 capture capacity in Fe_2O_3 and Fe system was higher compared with Fe_3O_4 and Fe system at the same conditions of pressure, temperature and reaction time. It was found that hematite quickly converts to magnetite during ball milling. Experimentally observed $FeCO_3$ decomposition temperature was above 300 °C. Magnetite, carbon and iron were identified as decomposition products. The sorbent material was used in four carbonation–calcination cycles showing good stability of CO_2 absorption capacity.

Conflicts of interest

The authors declare no conflicts of interest.

REFERENCES

[1] Saxena S, Kumar S. A comparative study of CO_2 sorption properties. Mater Renew Sustain Energy 2014, http://dx.doi.org/10.1007/s40243-014-0030-9.
[2] Bryant E. Climate process and change. Cambridge: Cambridge University; 1997.
[3] Yamauchi K, Murayama N, Shibata J. Absorption and release of carbon dioxide with various. Mater Trans 2007;48(10):2739–42.
[4] Brouwer J, Feron P. CO_2 absorption using precipitating amino acids in spray tower. In: 9th international CO_2 capture network meeting. 2006.
[5] Diao Y, Zheng X, Chen C. Experimental study on capturing CO_2 greenhouse gas by ammonia scrubbing. Energy Convers Manage 2004;45:2283–96.
[6] Chiesa P, Consonni S. Shift reactors and physical absorption. J Eng Gas Turbines Power 1999;121:295–305.
[7] Rochelle G. Amine scrubbing for CO_2 capture. Science 2009;325:1652–4.
[8] Merkel T, Lin H, Wei X. Power plant post-combustion carbon dioxide capture: an opportunity for membranes. J Membr Sci 2010;359:126–39.
[9] Cost performance baseline for fossil energy plants. Bituminous Coal 2007.
[10] Elwell L, Grant W. Technology options for capturing CO_2 – special reports. Power 2006;150(8).
[11] Shekhawat D, Luebke D, Pennline H. A review of carbon dioxide selective membranes – a topical teport. National Energy Technology Laboratory United States Department of energy; 2003.
[12] Bao L, Trachtenberg M. Facilitated transport of CO_2 across a liquid membrane:comparing enzyme, amine, and alkaline. J Membr Sci 2006;280:330–4.
[13] Li L, Wen X, Fu X, Wang F, Zhao N, Xiao F, et al. MgO/Al_2O_3 sorbent for CO_2 capture. Energy Fuels 2010;24:5773–80.
[14] Kumar S, Drozd V, Durygin A, Saxena S. Capturing CO_2 emissions in the iron industries using a magnetite–iron mixture. Energy Technol 2016, http://dx.doi.org/10.1002/ente.201500451.
[15] Salvador C, Lu D, Anthony E, Abanades J. Enhancement of CaO for CO_2 capture in an FBC environment. Chem Eng J 2003;96:187–95.
[16] Kim Y, Worrel E. International comparison of CO_2 emission trends in the iron and steel industry. Energy Policy 2002;30:827–38.
[17] Han K, Kyu C, Su Lee M. Performance of an ammonia-based CO_2 capture pilot facility in iron and steel industry. Int J Greenhouse Gas Control 2014;27:239–46.
[18] Rhee C, Kim J, Han K, Chun C. Process analysis for ammonia-based CO_2 capture in ironmaking industry. Energy Procedia 2011;4:1486–93.
[19] French B. Stability relations of siderite ($FeCO_3$), determined in controlled-fO_2 atmospheres. Maryland: Planetology Branch; 1970.
[20] Koziol A. Experimental determination of siderite (iron carbonate) stability under moderate pressure–temperature conditions, and application to martian carbonate parageneses. In: Lunar and Planetary Science XXX. 1999.
[21] Chai L, Navrotsky A. Enthalpy of formation of siderite and its application in phase equilibrium calculation. Am Mineral 1994;79:921–9.
[22] Das S, Kizilkanat A, Chowdhury S, Stone D, Neithalath N. Temperature-induced phase and microstructural transformations in a synthesized iron carbonate (siderite) complex. Mater Des 2016;92:189–99.
[23] Tao Zhou G. Synthesis of siderite microspheres and their transformation to magnetite microspheres. Eur J Mineral 2011, http://dx.doi.org/10.1127/0935-1221/2011/0023-2134.
[24] Alfe M, Ammendola P, Gargiulo V, Raganati F, Chirone R. Magnetite loaded carbon fine particles as low-cost CO_2 adsorbent in a sound assisted fluidized bed. Proc Combust Inst 2015;35:2801–9.
[25] Peterson S, Jackson M, Kim S, Palmquist D. Increasing biochar surface area: optimization of ball milling parameters. Powder Technol 2012;228:115–20.
[26] Yunfeng Z, Kaijun W, Jin H. Effect of ball milling on the properties of zirconia powder prepared by alcohol-aqueous coprecipitation method. Key Eng Mater 2013;544:34–7.
[27] Capus J. Metal powders—a global survey of production, applications and markets to 2010. Oxford: Elsevier; 2010.
[28] Gotor F, Macías M, Ortega A, Criado J. Comparative study of the kinetics of the thermal decomposition of synthetic and natural siderite samples. Phys Chem Miner 2000;27:495–503.
[29] Dhupe A, Gokarn AN. Studies in the thermal decomposition of natural siderites in the presence of air. Int J Miner Process 1990;28:209–20.
[30] Fosbol P, Thompsem K, Stenby E. Review and recommended thermodynamic properties of $FeCO_3$. Corros Eng Sci Technol 2013;115–135.
[31] Patterson J. A review of the effects of minerals in processing of Auatralian oil shales. Fuel 1994;73:321–7.
[32] Ten Brink H, Eenkhoorn S, Weeda M. The behavior of coal mineral carbonates in a simulated coal flame. Fuel Process Technol 1996;47:233–43.

[33] Luo Y, Zhu D, Pan J, Zhou X. Thermal decomposition behaviour and kinetics of Xinjiang siderite ore. Miner Process Extract Metall 2016;125:17–25.

[34] Ding J, Miao W, Pirault E, Street R, Mc Cormick P. Structural evolution of Fe + Fe$_2$O$_3$ during mechanical milling. J Magn Magn Mater 1998;177:933–4.

[35] Koziol M. Carbonate and magnetite parageneses as monitors of carbon dioxide and oxygen fugacity, XXXI. Dayton: Lunar and Planetary Science; 2000.

[36] French B, Rosemberg P. Siderite (FeCO$_3$): thermal decomposition in equilibrium with graphite. Science 1965;147:1284–5.

[37] Milesi V, Guyot F, Brunet F, Richard L, Benedetti RM, Dairou J, et al. Formation of CO$_2$, H$_2$ and condensed carbon from siderite dissolution in the 200–300 °C range and at 50 MPa. Geochim Cosmochim Acta 2015;54:201–11.

[38] Hammersley AP. ESRF internal report, ESRF97HA02T, FIT2D: an introduction and overview; 1997.

[39] Toby B. EXPGUI, a graphical interface for GSAS. J Appl Crystallogr 2001;34:210–21.

[40] Larson A, Von Dreele R. General structure analysis system (GSAS). In: Los Alamos National Laboratory Report LAUR; 2004. p. 86–748.

[41] Bale C, Chartrand P, Degterov S, Eriksson G, Hack K, Ben Mahfoud R, et al. FactSage thermochemical software and databases. Calphad 2002;26:189–228.

[42] Burgio N, Lassona A, Magini M, Martelli S, Padella F. Mechanical alloying of the Fe–Zr system. Correlation between input energy and end products. II Nuovo Cimento 1991;18(4):459–75.

[43] Kumar S. The effect of elevated pressure, temperature and particles morphology on the carbon dioxide capture using zinc oxide. J CO$_2$ Util 2014;8:60–6.

[44] Condon J. Surface area and porosity determinations by physisorption: measurements and theory. Amsterdam: Elesevier; 2006.

[45] Gheisari K, Javadpour S, Oh J, Ghaffari M. The effect of milling speed on the structural properties of mechanically alloyed Fe–45%Ni powders. J Alloys Compd 2009;472: 416–20.

[46] Zhang F, Zhu M, Wang C. Parameters optimization in the planetary ball milling of nanostructured tungsten carbide/cobalt powder. Int J Refract Met Hard Mater 2008;26:329–33.

[47] Sherif M, Aoki K, Sumiyama K, Suzuki K. Cyclic solid-state transformations during ball milling of aluminum zirconium powder and the effect and the effect high-energy planetary ball mill (Fritsch P5) equipped. Metall Mater Trans 1999;30:1877–80.

[48] Suryanarayana C. Mechanical alloying and milling. Prog Mater Sci 2001;46:1–184.

[49] Warne S. Differential thermal analysis of siderite-kaolinite mixtures. Am Mineral 1972;57:960–6.

[50] Wei RF, Cang DQ, Zhang LL, Bai YY. Staged reaction kinetics and characterization of iron oxide direct reduction by carbon. Int J Min Metall Mater 2015;22(10): 1025–32.

[51] Alkac D, Atalay U. Kinetics of thermal decomposition of Hekimhan-Deveci siderite ore sample. J Miner Process 2008;87:120–8.

[52] Hodkiewicz J. Characterizing carbon materials with Raman spectroscopy. Madison: Thermo Fisher Scientific; 2005.

[53] Reich S, Thomsen C. Raman spectroscopy of graphite. Philos Trans A Math Phys Eng Sci 2004;362:2271–8.